An Axisymmetric View of Concentric Eyewall Evolution in Hurricane Rita (2005)

MICHAEL M. BELL

Naval Postgraduate School, Monterey, California, and National Center for Atmospheric Research, Boulder, Colorado*

MICHAEL T. MONTGOMERY

Naval Postgraduate School, Monterey, California, and NOAA/AOML Hurricane Research Division, Miami, Florida

WEN-CHAU LEE

National Center for Atmospheric Research, Boulder, Colorado*

(Manuscript received 23 June 2011, in final form 1 December 2011)

ABSTRACT

Multiplatform observations of Hurricane Rita (2005) were collected as part of the Hurricane Rainband and Intensity Change Experiment (RAINEX) field campaign during a concentric eyewall stage of the storm's life cycle that occurred during 21–22 September. Satellite, aircraft, dropwindsonde, and Doppler radar data are used here to examine the symmetric evolution of the hurricane as it underwent eyewall replacement.

During the approximately 1-day observation period, developing convection associated with the secondary eyewall became more symmetric and contracted inward. Latent heating in the emergent secondary eyewall led to the development of a distinct toroidal (overturning) circulation with inertially constrained radial inflow above the boundary layer and compensating subsidence in the moat region, properties that are consistent broadly with the balanced vortex response to an imposed ring of diabatic heating outside the primary eyewall. The primary eyewall's convection became more asymmetric during the observation period, but the primary eyewall was still the dominant swirling wind and vorticity structure throughout the period.

The observed structure and evolution of Rita's secondary eyewall suggest that spinup of the tangential winds occurred both within and above the boundary layer, and that both balanced and unbalanced dynamical processes played an important role. Although Rita's core intensity decreased during the observation period, the observations indicate a 125% increase in areal extent of hurricane-force winds and a 19% increase in integrated kinetic energy resulting from the eyewall replacement.

1. Introduction

The eyewall of a mature tropical cyclone (TC) is a nearly circular ring of convection containing heavy precipitation and the strongest wind speeds in the storm. Observational evidence has long suggested that once a TC has reached a sufficient intensity, it may form a secondary eyewall outside the primary one, resulting in one or more concentric rings of convection and a weakening of the primary vortex (Willoughby et al. 1982; Houze et al. 2007, and references therein). Because of an incomplete understanding of the underlying dynamics and thermodynamics of secondary eyewall formation and evolution, forecasts of intensity change related to eyewall replacement are still inadequate. Our incomplete understanding of the phenomenon is compounded by a lack of detailed observations of the eyewall replacement process and the exceptional timing and coordination of aircraft flights that is required. One noteworthy example of successful observations obtained from aircraft data is the case of Hurricane Gilbert's (1988) double eyewall structure and kinematics (Black and Willoughby 1992; Dodge et al. 1999). These data were nonetheless limited in their ability to clearly discern the dominant mesoscale processes controlling the eyewall replacement.

The Hurricane Rainband and Intensity Change Experiment (RAINEX) flights in Hurricane Rita (2005)

* The National Center for Atmospheric Research is sponsored by the National Science Foundation.

Corresponding author address: Michael M. Bell, 589 Dyer Road, Root Hall, Room 254, Monterey, CA 93943.
E-mail: mmbell@nps.edu

DOI: 10.1175/JAS-D-11-0167.1

were the first to extensively observe an eyewall replacement with the Electra Doppler radar (ELDORA; Houze et al. 2006). Houze et al. (2007) and Didlake and Houze (2011) presented the mesoscale structure of Rita's concentric eyewalls derived from RAINEX data, and in this work we more fully explore this dataset by examining the time evolution of Rita's eyewall replacement. As a first step to understanding concentric eyewall evolution, this study focuses on the collective effects of rotating deep convective structures as represented by the azimuthal average of the observed three-dimensional state variables. Although recent work indicates that the intensification process is inherently three-dimensional (Nguyen et al. 2008), the axisymmetric "mean-field" view still provides a useful vantage point for understanding the system-scale aspects of the intensification process (Montgomery and Smith 2011, manuscript submitted to *Quart. J. Roy. Meteor. Soc.*) and eyewall replacement process in particular.

Building on Eliassen's (1952) pioneering work examining the slow meridional circulation of the zonally symmetric general circulation driven by heat and momentum forcing, Willoughby (1979), Shapiro and Willoughby (1982), and Schubert and Hack (1982, 1983) developed an analogous mathematical framework for studying the slow axisymmetric evolution of a circular hurricane vortex in gradient and hydrostatic balance subject to heat and tangential momentum forcing. To maintain a state of gradient and hydrostatic balance, the theory furnishes a diagnostic differential equation for the transverse streamfunction in the radius–height plane. This equation and its inversion for the streamfunction, along with the corresponding tendency equations for tangential momentum and potential temperature, will be referred to here as the Eliassen balance model (EBM). The EBM has proven useful for interpreting hurricane observations (Willoughby et al. 1982) and cloud-representing numerical simulations of tropical cyclogenesis (Hendricks et al. 2004; Montgomery et al. 2006b; Fudeyasu et al. 2010; Fang and Zhang 2010) and intensification (Bui et al. 2009; Fudeyasu and Wang 2011).

In the EBM, a tangential momentum sink (i.e., drag at the sea surface) forces a streamfunction gyre with inflow through the source and compensating outflow above it, with upward motion radially inward of the momentum sink. A heat source (i.e., condensational heating in a convective ring) forces a mesoscale updraft through the source, with compensating downdrafts radially inward and outward. A ring of heating that is strongest at middle levels will thus drive an inflow toward the ring at low levels and away from the ring at upper levels. We will suggest here that the observed evolution of the axisymmetric secondary circulation derived from the ELDORA radar data can be described to first order by the balanced response to changes in heating and vorticity in two concentric rings.

A weak toroidal (overturning) circulation associated with the incipient secondary eyewall will be shown to develop into a strong toroidal circulation, which is distinct from that of the primary eyewall. An increase in the depth of the radial inflow at the secondary eyewall is argued to be associated with an increase in azimuthally averaged heating as the convective ring becomes more symmetric. The formation of an eyelike "moat" has been proposed to be the result of forced subsidence from both eyewalls combined in a region of strong inertial stability and rapid filamentation of convection (Rozoff et al. 2006). Quad-Doppler radar analysis and flight-level data will provide evidence for deep subsidence and strong radial shear of the tangential wind in the moat region.

Ooyama (1982) argued that the mechanism of intensification was in association with the thermally driven radial inflow in a deep layer, in conjunction with conservation of absolute angular momentum M.[1] Smith (1981), Schubert and Hack (1982), and Shapiro and Willoughby (1982) developed the mechanism further, deriving mathematical expressions for the contraction and amplification of a tangential wind maximum by latent heat release near the radius of maximum winds (RMW). Smith et al. (2009) and Montgomery and Smith (2011, manuscript submitted to *Quart. J. Roy. Meteor. Soc.*) showed that thermally driven radial inflow is only one of two axisymmetric mechanisms for spinning up the mean vortex. In this paper we define the "first mechanism" as the radial convergence of M above the boundary layer produced by the balanced secondary circulation in response to the collective effects of diabatic heating in a ring of rotating deep convection. This mechanism was also proposed to explain how the mean vortex can expand in size. We define the "second mechanism" as an additional spinup of the tangential winds within the boundary layer in the inner-core region of the storm due to unbalanced dynamics. The spinup is also associated with radial convergence of M, but in the second mechanism the convergence occurs in the boundary layer where M is not materially conserved because of frictional torque. In the absence of diabatic heating (i.e., the first mechanism) this torque leads to a spindown of the boundary layer flow. Spinup of the boundary layer flow can occur when the radial inflow is sufficiently large to converge rings of air to small radii with minimal loss

[1] The azimuthally averaged absolute angular momentum in cylindrical coordinates is given by $\overline{M} = r\overline{v} + fr^2/2$, where r denotes the radius from the system center, f denotes the Coriolis parameter, and $\overline{v}$ denotes the azimuthally averaged tangential velocity.

of M. Supergradient winds that exceed the tangential velocity at the top of the boundary layer produce an agradient force that decelerates the radial inflow at the eyewall and can support deep convection and further intensification via the first mechanism. Both intensification mechanisms were originally presented in the context of the spinup of the primary vortex, but Huang et al. (2012) showed that these concepts are also applicable to the spinup of the secondary eyewall in a numerical simulation of Typhoon Sinlaku (2008). The RAINEX analyses presented herein will be shown to be consistent with this new interpretation, providing observational evidence that these two axisymmetric mechanisms provide a useful framework for understanding concentric eyewall evolution.

An outline of the remaining paper is as follows. An overview of observing systems employed in the RAINEX experiment, analysis techniques, and general storm information is presented in section 2. Satellite, in situ, and Doppler radar analyses are combined in section 3 to illustrate the concentric eyewall evolution over the 1-day intensive observing period (IOP). Section 4 uses the dropsonde data to examine the kinematics and thermodynamic structure of the boundary layer. A discussion of these results and open questions are detailed in section 5. A summary of the main findings is given in section 6.

2. RAINEX observations

a. Observing systems

The RAINEX field campaign was conducted from Tampa and Miami, Florida, during August and September 2005 to study the dynamics and interactions of the eye, eyewall, and rainbands [see Houze et al. (2006) for a detailed summary of scientific objectives]. Research and operational aircraft missions were conducted with National Oceanic and Atmospheric Administration WP-3D (NOAA P-3), Naval Research Laboratory WP-3D (NRL P-3), and U.S. Air Force (USAF) C-130 turboprop aircraft. Axisymmetric kinematic quantities were obtained by azimuthally averaging data from two primary flight patterns. The ''figure-four'' pattern consists of straight-line segments through the TC center in the four storm quadrants and a connecting pass that gives the pattern a resemblance to the numeral 4. The figure-four pattern provided direct in situ measurements along radial lines from the center. The ''circumnavigation'' pattern, where the aircraft flew azimuthally around the eyewall, provided in situ data along an outer radius. Both patterns provided remotely sensed radar data in the inner core.

All aircraft were equipped with flight-level temperature, humidity, and pressure sensors, and global positioning system (GPS) dropwindsondes (hereafter dropsondes; Hock and Franklin 1999). Flight-level and dropsonde data were inspected and quality-controlled to remove noise and other instrument errors. Pseudoequivalent potential temperature θ_e was calculated following the empirical formula in Bolton (1980). The Zipser et al. (1981) correction for minor wetting errors was applied to supersaturated observations in the in situ data. This correction was shown by Eastin et al. (2002) to reduce the majority of significant instrument wetting errors but not remove them completely, resulting in an average θ_e error of 2–3 K.

Dropsonde data were the only observations available for documenting the kinematic and thermodynamic structure of the boundary layer. In this paper, a dynamically apt definition of the boundary layer and its top are employed as suggested by Smith and Montgomery (2010) and Zhang et al. (2011). The boundary layer is defined as the layer of strong radial inflow that is significantly out of gradient wind balance; the top of the boundary layer is defined as the height at which the mean radial inflow diminishes to a small fraction (e.g., 10%) of the maximum inflow near the surface. The boundary layer height is found to be at approximately 1-km altitude at both the primary and secondary eyewall on both analysis days.

Each of the P-3 aircraft had Doppler X-band (~3 cm) tail radars (Hildebrand et al. 1996; Jorgensen et al. 1996), and the NOAA P-3 had an additional C-band (~5 cm) lower-fuselage (LF) radar. Doppler syntheses were limited in range and time to minimize degradation of highly resolved, short-range radar data that was also observed at long range at different times in a flight pattern. Traditionally, airborne Doppler radar data are collected with the aircraft flying a straight line pattern, yielding an approximate 30° separation of two radar beams from the antennas that point ±15° from normal to the ground track of the aircraft (Hildebrand et al. 1996). One result of flying curved tracks in a circumnavigation flight pattern is that there is a decrease in wind uncertainty toward the center of the tropical cyclone, with a corresponding increase in uncertainty radially outward as radar beams fan apart due to the change in dual-Doppler geometry. A minimum angle separation between Doppler radials of 15° was therefore enforced.

The figure-four and circumnavigation flight patterns provide complementary radar observations; the best-resolved wind components from the Doppler synthesis are reversed in the two flight patterns, with the lowest velocity uncertainty in the cross-track direction (e.g., tangential velocity in the figure four, and radial velocity in the circumnavigation). When available, Doppler data from multiple aircraft flying these two patterns together provide the best geometry for synthesis. This combined analysis is referred to as ''quad-Doppler'' (Jorgensen et al. 1996), and this method is used in section 3b below.

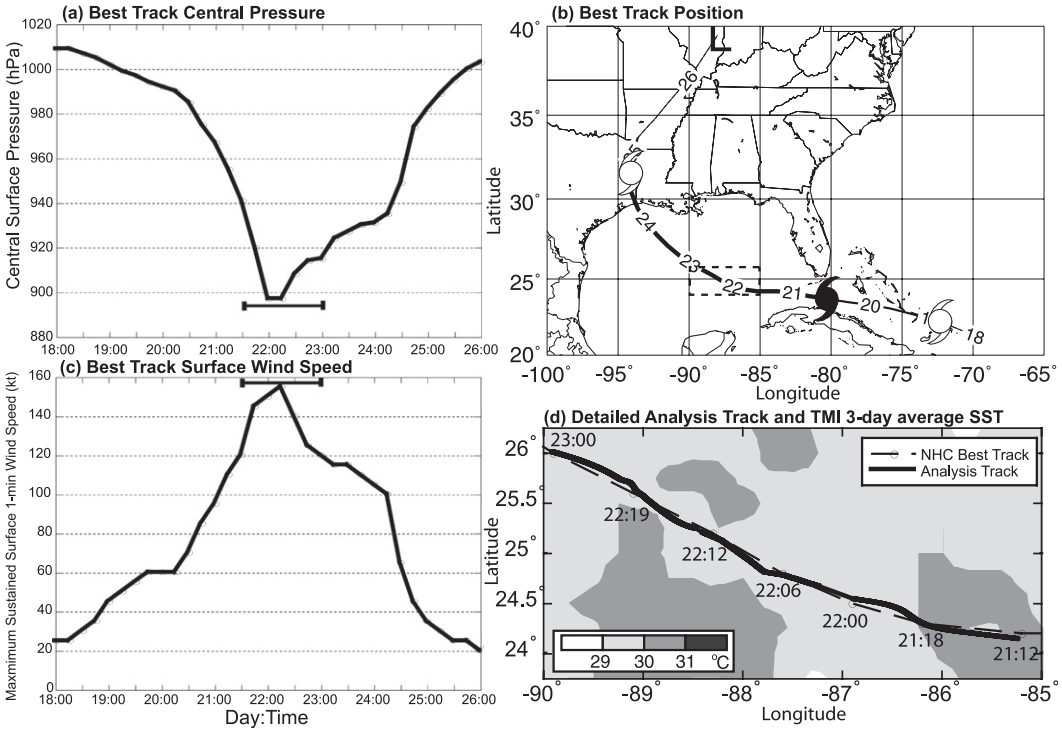

FIG. 1. Hurricane Rita (2005) track, intensity, and SST. (a),(c) National Hurricane Center best-track intensity, measured by (a) central surface pressure and (c) maximum sustained 1-min surface wind speed, with the bracketed line indicating times shown in (d). (b) Best-track position, with the open hurricane symbol denoting tropical storm strength, the closed symbol denoting hurricane strength, and L denoting a remnant low. The dashed box indicates the area shown in (d). (d) The detailed analysis track along with the best track, and 3-day averaged SST ending on 21 September derived from the Tropical Rainfall Measuring Mission (TRMM) Microwave Imager (TMI).

Airborne radar data were edited using the National Center for Atmospheric Research (NCAR) Solo software to correct navigation errors and remove noise and ocean returns (Oye et al. 1995; Bosart et al. 2002). The synthesized data from the fore and aft pointing radar beams provided three-dimensional precipitation and kinematic structures. Cartesian wind syntheses were obtained from multiple Doppler velocities using a variational approach (Gao et al. 1999; Reasor et al. 2009; Houze et al. 2009). The wind fields were synthesized at 600-m grid spacing for ELDORA only and at 1.5 km for quad-Doppler ELDORA/NOAA analysis. The wind fields were then smoothed with a low-pass filter to yield resolvable horizontal wavelengths of 2.4 and 6 km, respectively, to remove grid-scale noise prior to the calculation of vertical vorticity.

b. Hurricane Rita

Figure 1 shows the National Hurricane Center (NHC) best-track and analysis track detail for Hurricane Rita. The TC was named as a tropical storm at 1800 UTC 18 September near the Bahamas, and intensified to a category 5 hurricane in the Gulf of Mexico during the next 3 days (Beven et al. 2008). The peak intensity of 80 m s^{-1} (defined as the maximum 1-min sustained surface wind) is estimated to have occurred between aircraft missions at 0300 UTC 22 September (Fig. 1b), with an 895-hPa central pressure (Fig. 1a). RAINEX missions on 19, 21, 22, and 23 September captured much of the mature storm phase, including a concentric eyewall event on 21–22 September. Additional data were collected by operational reconnaissance flights because of the hurricane's threat to land. This paper focuses on the roughly 24-h period beginning at about 1800 UTC 21 September highlighted in Fig. 1. During this period, a secondary eyewall formed as the storm peaked in intensity. Figure 1d shows the detailed analysis track used for azimuthally averaging the RAINEX dataset. The analysis track was determined by a cubic spline fit to circulation centers that maximize the tangential wind in a 3-km annulus centered at the RMW when radar data were available (Marks et al. 1992) or from aircraft center fixes when radar data were not available. The estimated center error of the analyzed track is less than 3 km.

The environment during this period was favorable for intensification, with warm sea surface temperatures (SSTs)

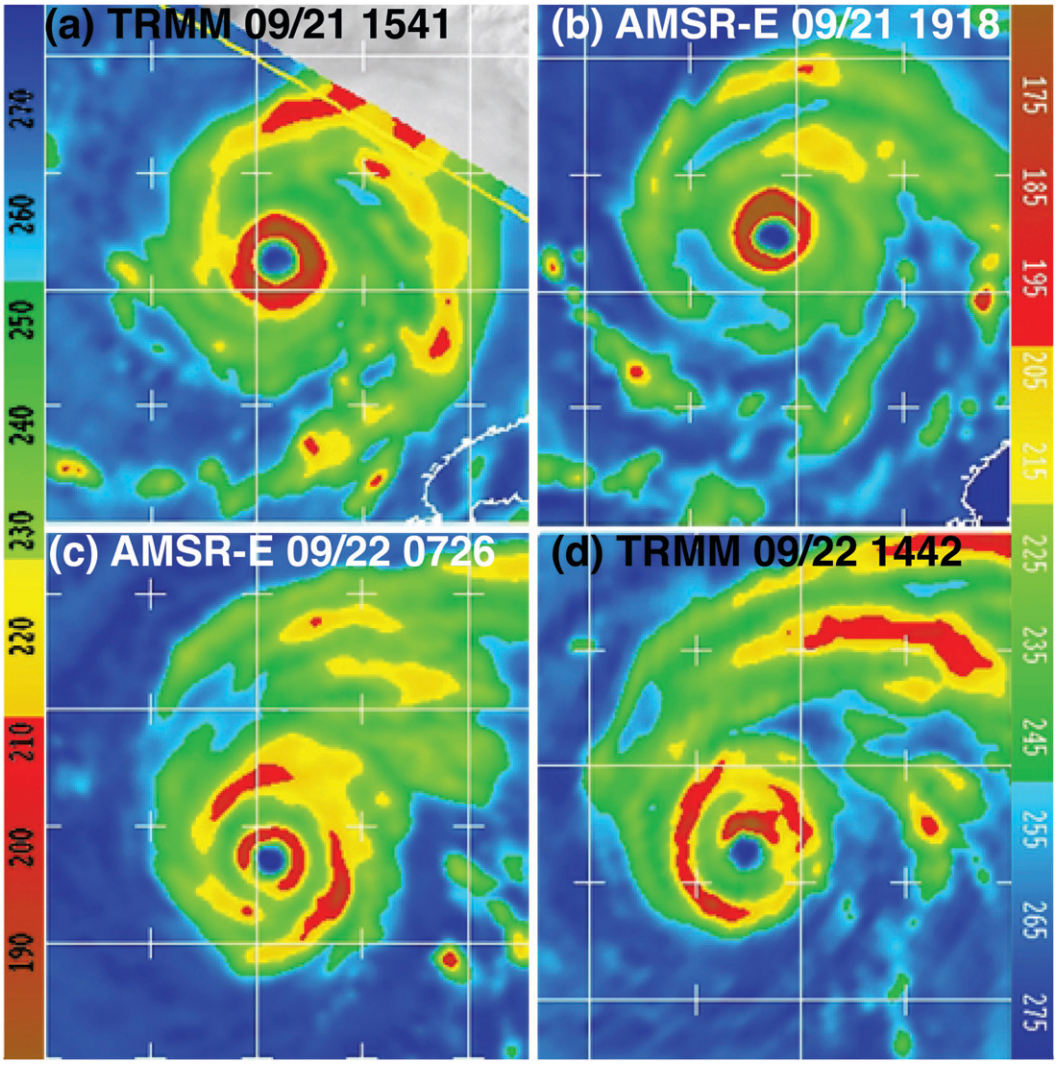

FIG. 2. Brightness temperatures from (a),(d) TRMM/TMI (at 85 GHz) and (b),(c) *Aqua*/AMSR-E (at 89 GHz) polar-orbiting microwave satellites at four consecutive times. Color scales on left and right correspond to TRMM and AMSR-E temperatures, respectively. White tick marks are every 1° with solid white lines every 2° of latitude and longitude.

near 30°C (Fig. 1d) and low to moderate vertical shear. The estimated average magnitude of the vector difference between the winds at 200 and 850 hPa was about 5 m s^{-1} from 214° using European Centre for Medium-Range Weather Forecasting (ECMWF) analyses and the method described by Corbosiero and Molinari (2002), but it increased near the end of the period.

3. Concentric eyewall evolution

a. Convective characteristics

Changes in precipitation structure have been one of the primary indicators of eyewall replacement, partly due to the relatively frequent availability of satellite imagery (Hawkins and Helveston 2008). The scattering of high microwave frequencies (85–89 GHz) by large or numerous ice particles lofted to high altitude by deep convection in the eyewall region produces low brightness temperatures detected by spaceborne passive remote sensors (Fig. 2). Four consecutive passes by the Tropical Rainfall Measuring Mission (TRMM) Microwave Imager (TMI) and Advanced Microwave Scanning Radiometer–Earth Observing System (AMSR-E) satellites illustrate the evolution from a single to concentric eyewall. In Fig. 2a, the two prominent features are the circular eyewall and large primary rainband extending outward from the center. The structure of this primary rainband was described by Hence and Houze (2008). Figure 2b shows that the convection in the primary rainband had weakened about 3.5 h later, but the primary

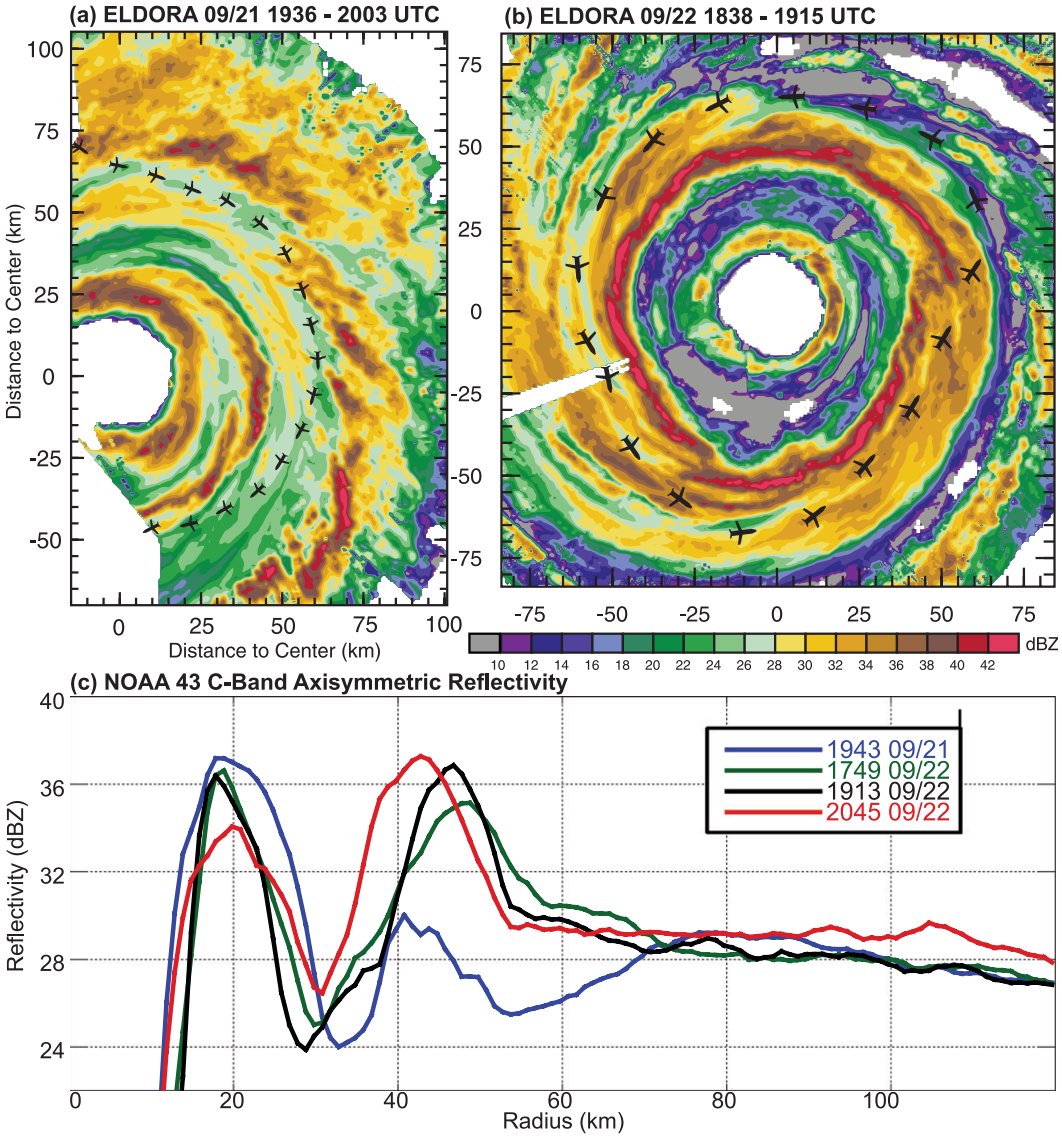

FIG. 3. Radar reflectivity from ELDORA X-band at 3-km altitude during (a) 1936–2003 UTC 21 September and (b) 1838–1915 UTC 22 September, and (c) axisymmetric reflectivity from NOAA C-band at ~3 km at four consecutive times shown in inset.

eyewall remained intense and symmetric. The origins of the secondary eyewall are nonetheless evident in Fig. 2b, with low brightness temperatures in the northeast quadrant of the storm. By 0726 UTC the next day (Fig. 2c), both eyewalls were well developed and approximately concentric, but both convective rings were open to the southwestern side. This image was taken only a few hours after Rita reached maximum intensity. Seven hours later (Fig. 2d), the original eyewall had begun to deteriorate while its replacement had intensified.

The 85-GHz passive microwave satellite imagery provides valuable snapshots of the storm structure at about 5-km pixel resolution, but airborne precipitation radars reveal an even higher-resolution depiction of this structure at a 600-m grid resolution through active remote sensing at close range. The radar reflectivities at 3-km altitude from the beginning and end of the analysis period are shown in Figs. 3a,b. The roughly 23-h separation between the analyses reveals significant changes in Rita's convective characteristics. Three primary areas of high echo intensity are evident at 1936 UTC 21 September (Fig. 3a): the primary circular eyewall; an intense spiral band located about 40 km east and southeast of the storm center that becomes tangent to the eyewall north of the storm center; and a broad quasi-circular rainband at 75-km radius. The cellular, streaklike nature

of the rainband at 75-km radius is evident in the higher spatial resolution airborne radar observations compared to the satellite imagery.

Data obtained from a circumnavigation around the secondary eyewall at 1838 UTC 22 September are shown in Fig. 3b. In contrast to the previous day, the radar echo was characterized by sharp radial delineations between azimuthally contiguous convective elements and low-reflectivity regions. During this period, the secondary eyewall was the dominant feature in the reflectivity field, with an almost continuous band of reflectivity exceeding 40 dBZ. The primary eyewall appears to have deteriorated on its southwestern side, although some of the apparent structure is due to attenuation and convective evolution that occurred during the circumnavigation flight pattern. The moat region of low reflectivity between the two eyewalls indicates a dipole pattern of ascent and subsidence. A more detailed dynamical interpretation for this dipole pattern is discussed in section 3b.

Attenuation at X band can be substantial in heavy precipitation, limiting the returned power on the far side of a hurricane rainband. Analysis of a previous time period where the NRL P-3 flew in the moat region (cf. Houze et al. 2007; Didlake and Houze 2011) suggests that the primary eyewall reflectivity is attenuated in both Figs. 3a and 3b. Independent reflectivity measurements obtained by the NOAA P-3 LF C-band radar were used to improve the estimate of the axisymmetric reflectivity. The 5-cm wavelength data complement the 3-cm radar analysis with increased range and less attenuation, but the larger 4.1° vertical beamwidth (vs. 1.8°) and fixed elevation angle still limit the quantitative information at longer range. To composite the best estimate of the reflectivity, the maximum values at polar grid points with 1-km radial and 0.5° azimuthal resolution were used in an azimuthal average (Marks 1985). Data were limited to a 30-min window around the aircraft's closest point of approach to the center to minimize range issues.

Axisymmetric reflectivity from the lower fuselage radar near 3-km altitude at several key times is shown in Fig. 3c. The figure illustrates that the reflectivity in the secondary eyewall increased in magnitude and contracted radially inward, while the reflectivity in the primary eyewall gradually decreased. Three maxima at similar radii to those described in Fig. 3a are found at 1943 UTC 21 September (blue curve), near the time of the ELDORA circumnavigation. The weak maximum near 80 km appears to underestimate the reflectivity due to beam spreading and elevation. By 1749 UTC the next day when a NOAA P-3 returned to Rita, the outer maximum near 80-km radius appears to have contracted about 30 km and intensified (green curve). A continued contraction occurred at a rate of about 1.5 km h^{-1} as the secondary reflectivity maximum equaled, and then surpassed, the primary ring after 1749 UTC (black and red curves). The moat region gradually became rain-free, consistent with the ELDORA reflectivity shown in Fig. 3b. It is not possible to track reflectivity over the long period between radar coverage, but the estimated contraction rate deduced from the consecutive passes on 22 September (green, black, and red curves) suggests temporal continuity of the reflectivity maxima at 80 km (blue curve, Figs. 3a and 6a) and 30 km (black curve, Figs. 3b and 6b). While the exact magnitude of the precipitation changes is uncertain due to radar attenuation and beam spreading, the ELDORA and the NOAA LF radar reflectivities are consistent in their depiction of the developing convection-free moat and the increasing azimuthal symmetry of the outer convective ring.

b. Kinematic evolution

1) 700-hPa in situ analysis

In situ data from consecutive C-130 and NOAA P-3 figure-four flight patterns were azimuthally averaged to deduce the kinematic structure at 700 hPa (~3 km). The data were averaged on a 1.5-km radial grid over the roughly 3-h duration of each figure four. The radial profiles of storm-relative tangential wind were smoothed after averaging with a one-dimensional low-pass filter (Leise 1982) that removed wavelengths less than 12 km and associated noise in order to focus on mesoscale evolution. The azimuthal mean absolute angular momentum $\overline{M}$ and vertical vorticity were then calculated from the smoothed mean wind fields. In symmetric polar coordinates, the absolute vertical vorticity is equal to one over radius times the radial gradient of the absolute angular momentum. The azimuthal mean absolute vertical vorticity can be partitioned into three terms as $\overline{\eta} = \overline{v}/r + \partial\overline{v}/\partial r + f$, where $\overline{\eta}$ denotes the absolute vertical vorticity, $\overline{v}/r$ denotes the curvature vorticity, $\partial\overline{v}/\partial r$ denotes the shear vorticity, and f denotes the (assumed constant) Coriolis parameter, or planetary vorticity. The overbar represents an azimuthal average. A figure-four flight track and tangential winds from a representative flight pattern centered at about 0630 UTC are shown in Fig. 4. The scale-filtered tangential winds (black line) are smoother than the direct azimuthal average (red line) of the noisier raw data (dots). The filtering reduces the local vorticity amplitude but retains coherent mesoscale kinematic structures. Six consecutive estimates of the mesoscale axisymmetric wind structure similar to that shown in Fig. 4 were obtained over a 24-h period, with a 5-h gap from 0000 to 0500 UTC. The resulting profiles were then linearly interpolated in time to produce a time series plot of vertical vorticity (color), tangential wind (thin white contours), and M

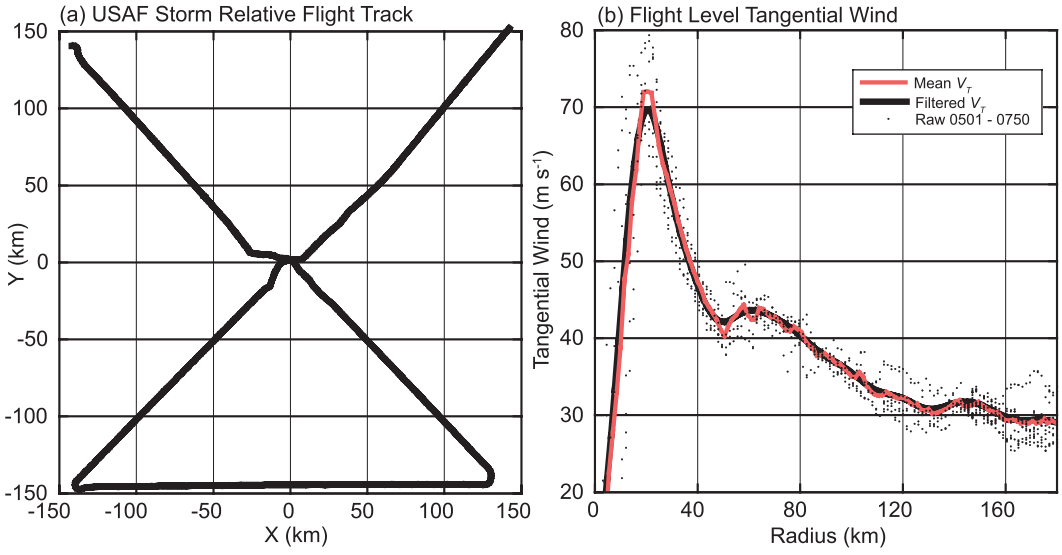

FIG. 4. U.S. Air Force flight track and tangential wind from 0501 to 0750 UTC 22 Sep. (a) The storm-relative "figure four" flight track used to compute the azimuthal mean structure. (b) The tangential wind V_T (m s^{-1}) from the raw in situ data (dots), azimuthal mean (red line), and scale filtered mean (black line).

(thick yellow contours) from 1830 UTC 21 September to 1830 UTC 22 September shown in Fig. 5.

The kinematic time series at 700-hPa altitude shows a contraction and peak in intensity of the primary eyewall, the development and contraction of the concentric eyewall, and an expansion of the tangential wind field. The mesoscale-filtered primary tangential wind maximum increased to about 70 m s^{-1} and the RMW contracted to about 22 km during the first 12 h. The primary tangential wind maximum gradually weakened without further contraction for the remainder of the period. The weakening in the latter period is consistent with the convective evolution inferred from Figs. 2 and 3, with a deterioration of the primary eyewall convection after 0700 UTC. However, the primary eyewall remains the dominant kinematic feature throughout the period, with a distinct ring of vertical vorticity on the inner edge of the RMW that is more than 4 times greater than the secondary eyewall even at the end of the period. The intense primary vortex sheet exceeded 8×10^{-3} s^{-1} at its peak, and weakened only slightly in the latter half of the time series.

In Fig. 5, the secondary eyewall appears to have emerged from the region near 80-km radius, suggesting that the rainband evident in this region was the nascent secondary

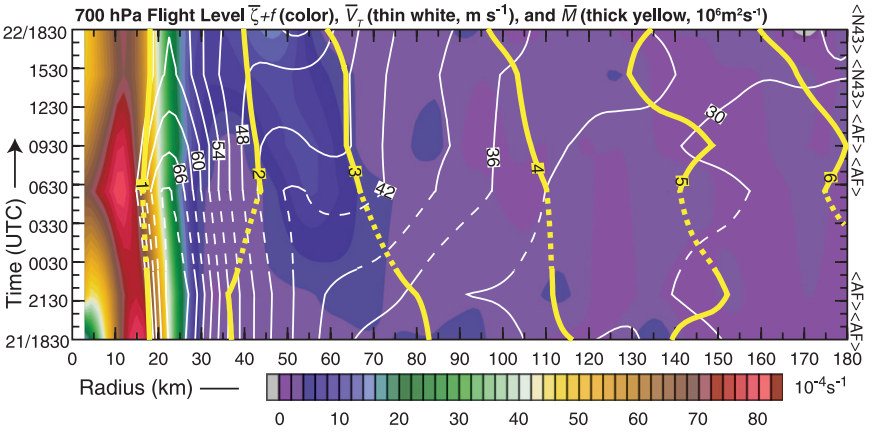

FIG. 5. Radial time series of mesoscale-filtered axisymmetric absolute vertical vorticity (color, 10^{-4} s^{-1}) and tangential wind (contour, m s^{-1}) at 700-hPa flight level from 1830 UTC 21 Sep to 1830 UTC 22 Sep. Aircraft passes corresponding to analysis times are shown on the right ordinate. Dashed contours indicate linearly interpolated data between aircraft missions.

eyewall. The region near 80-km radius is characterized by a relatively weak radial gradient of tangential wind that results in a ''tangential-wind plateau,'' where curvature vorticity dominates over the negative shear vorticity. Building off of a body of work recognizing the importance of the axisymmetrization process in intense geophysical vortices (e.g., Melander et al. 1987; Shapiro and Montgomery 1993), Rozoff et al. (2006) suggested that convective air parcels and their associated vertical vorticity anomalies would be deformed into filaments by stretching and shearing deformations in strain-dominated regions. They argued that the persistence of convection would be more likely where the ''filamentation time'' τ_{fil} is greater than a convective time scale of approximately 30 min. Estimates of this parameter indicate τ_{fil} is less than 30 min inside of 60-km radius but is greater than 2 h near 80-km radius (not shown). Dropsonde soundings indicate that the atmosphere in this region was conditionally unstable and thermodynamically favorable for convection (see Fig. 9d).

Unfortunately, the data gap between 0000 and 0500 UTC indicated by the dashed contours precludes direct tracking of the initial secondary vorticity and wind speed maxima through the period identified by the National Hurricane Center as maximum intensity (~0300 UTC). Stronger maxima in the primary eyewall and/or initiation of new secondary maxima may be missing from the time series during this gap. A velocity inflection point and local wind speed maximum were apparent near 60-km radius at 0500 UTC when the aircraft returned after the 5-h data gap. The wind speed increased at the secondary radius of maximum winds (SRMW) to nearly 51 m s^{-1} at the end of the analysis period. The SRMW had an average contraction rate of about 1 km h^{-1}, with a maximum rate of 2.5 km h^{-1}, which is broadly consistent with the reflectivity contraction shown in Fig. 3. The time series also indicates that the vertical vorticity following the SRMW increased throughout the period, with an average rate of about 5×10^{-5} s^{-1} h^{-1}. While the quantitative rates of change are admittedly crude given the filtering and temporal interpolation, the end result was an approximate 30-km contraction of the SRMW and tripling of the maximum vorticity following the SRMW over 24 h.

The enhancement of vorticity at the SRMW can also be discerned from the radial displacement of the M surfaces, with convergence of the 2 and 3×10^6 m^2 s^{-1} contours near 50-km radius. The time series indicates that the M surfaces near the developing secondary eyewall were becoming more tightly packed over time, sharpening the radial momentum gradient in an analogous manner to thermodynamic frontogenesis (Emanuel 1997). All M surfaces with values larger than 3×10^6 m^2 s^{-1} moved radially inward over the analysis period. Radial velocities at this altitude were on the order of a few meters per second (not shown), suggesting the vortex was nearly in gradient balance at 700 hPa and implying that balance dynamics is an appropriate zero-order framework for interpreting the results above the boundary layer (Shapiro and Willoughby 1982). We hypothesize that the radial convergence of the M surfaces was largely due to the balanced response to increased diabatic heating in the secondary eyewall. The reversal of the radial movement from inward to outward of the 2×10^6 m^2 s^{-1} surface at 2130 UTC, followed by a weaker reversal of the 1×10^6 m^2 s^{-1} surface at 0930 UTC, is consistent with this hypothesis.

The radial convergence of M resulted also in an expansion of the area of damaging surface winds. Using an 85% surface reduction factor (Franklin et al. 2003), we see that the azimuthally averaged radius of hurricane-force winds (33 m s^{-1} at the surface, ~39 m s^{-1} at 700 hPa) increased from 60 to 90 km, resulting in a 125% increase in area of hurricane-force winds. The radius of gale force winds (25.7 m s^{-1} at the surface, ~30.6 m s^{-1} at 700 hPa) increased from 160 to beyond 180 km, but limited data beyond this range prohibit sufficient averaging. This indicates an areal increase of at least 25%. This relatively rapid expansion of the outer wind field has a significant impact for maritime activities, including military operations (Elsberry and Stenger 2008) and commercial shipping, as well as increased damage potential at landfall. One can also quantify the effect of the outer wind increase by integrating the kinetic energy $\int[\rho(u^2+v^2)/2]rdrd\lambda$ from the center to the edge of the domain on the 700-hPa surface, yielding a 19% increase over these 24 h. Despite the reduction in intensity as defined by the maximum sustained 1-min surface wind, Rita increased in size and strength over this period (Powell and Reinhold 2007; Maclay et al. 2008).

2) ELDORA ANALYSIS

The azimuthally averaged kinematic fields from the ELDORA analysis at 1936 UTC 21 September are shown in Fig. 6a. Sea clutter and lack of scatterers prevent analysis in the lowest levels and in the eye. The kinematics are dominated by the primary eyewall with mean tangential wind velocities exceeding 75 m s^{-1} and radial outflow in most of the middle and lower troposphere. The intense vortex sheet at the primary eyewall slopes outward and is coupled to the convection in the eyewall (see Fig. 3a) with a central updraft of 8 m s^{-1}, and a ring of vorticity exceeding 8×10^{-3} s^{-1} that is consistent with calculations from the in situ data. The outflow layer in the upper troposphere is collocated with weakly anticyclonic vorticity due to the nearly horizontal angular momentum surfaces. It is unclear whether this

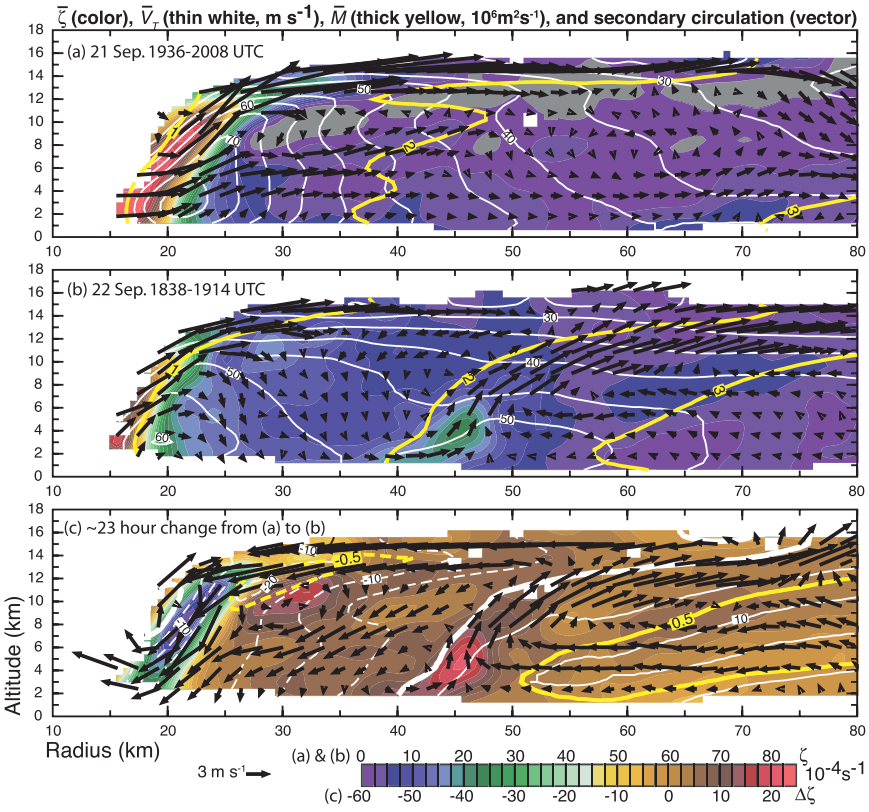

FIG. 6. Axisymmetric relative vorticity (color, 10^{-4} s^{-1}), tangential wind (contour, m s^{-1}), and secondary circulation (vector) derived from ELDORA. (a),(b) Flight patterns and times shown in Fig. 1, and (c) the change between the two analysis times. Dashed contours in (c) indicate a negative change of tangential wind and absolute angular momentum, thick contours indicate zero change, and solid contours indicate positive change. Vorticity change in (c) is indicated by the numbers on the bottom of the color bar.

is representative of inertial instability or uncertainty in the wind analysis. The transverse circulation generally follows the angular momentum surfaces, suggesting that M is approximately conserved throughout most of the domain.

Two additional regions of enhanced vertical vorticity are found slightly radially inward of the convective regions shown previously in Fig. 3a. The outermost vorticity maximum near 70-km radius exceeds 6×10^{-4} s^{-1}, approximately one order of magnitude greater than the Coriolis parameter at this latitude. Low-level convergence is evident at this radius, associated with two counterrotating secondary circulations on the inner and outer sides of the vorticity maximum. The updraft in this region is much shallower than the one found in the primary eyewall. Evidence of the tangential-wind plateau is seen in this region, with perhaps an outward tilt with height. The low-level vertical vorticity maximum near 40 km is slightly weaker than the vorticity maximum at 70-km radius and does not appear to have a distinct secondary circulation associated with it. The azimuthally averaged reflectivity in the band at 45 km is also weaker than the band at 75 km (not shown).

The lack of available ELDORA data in the southwest quadrant at this time suggests that the azimuthally averaged tangential wind speeds are an overestimate, especially in the primary eyewall. The in situ and dropsonde data suggest that the maximum azimuthally averaged tangential wind speed was closer to 70 m s^{-1} at the top of the boundary layer. It is doubtful, however, that inclusion of data from the left rear quadrant would fundamentally change our conclusions about the origin of the secondary eyewall. The radar analysis is generally consistent with the in situ analysis at this time and provides some additional evidence that the outer rainband was the precursor to the secondary eyewall.

By 1838 UTC the next day, about 23 h later, the secondary eyewall has matured (Fig. 6b). The primary eyewall is still the dominant dynamical feature, but a concentric ring of vorticity at about 45 km now exceeds 2.5×10^{-3} s^{-1}.

The transverse circulation now shows two distinct outflow channels originating near the top of the storm, with downward motion between the two eyewalls in the moat region. The 2×10^6 m^2 s^{-1} M contour has moved radially outward and has a radially inward bulge near the base of the secondary eyewall at the leading edge of a comma-shaped vorticity maximum. The inward bulge of M and enhanced low-level radial outflow at the secondary eyewall are believed to be associated with supergradient winds in the boundary layer. Smith et al. (2008, 2009) argued that an intrinsic gradient wind imbalance in the boundary layer produces an overshoot/adjustment region on the innermost edge of an eyewall. If the winds are supergradient as they rise upward out of the boundary layer, they must flow radially outward as they adjust toward gradient wind balance. The Doppler wind analyses in Fig. 6b are consistent with the Smith et al. (2008, 2009) hypothesis, and are further supported by the dropsonde analyses in the boundary layer presented in section 4.

The shallow toroidal secondary circulation associated with the rainband at 75-km radius on the previous day now extends throughout the depth of the troposphere, with an outwardly tilted axis of toroidal rotation that approximately parallels the 2×10^6 m^2 s^{-1} M contour. A tilted column of convergence exceeding 5×10^{-4} s^{-1} up to 10-km altitude is found along the radially outward side of this axis (not shown). This convergence was increasing vertical vorticity in a deep column at the leading edge of the convection through vortex tube stretching. Tilting of horizontal vorticity associated with vertical shear of the tangential wind is a maximum near the inner edge of the band near 40-km radius in the middle troposphere where the vertical velocity changes sign, which may also have contributed to the ''comma'' shape of the vorticity maximum.

The depth of the inflow into the secondary eyewall extends to nearly 9-km altitude at 70-km radius. This is accompanied by a significant change in the position of the 3×10^6 m^2 s^{-1} M contour throughout the low to midtroposphere. A region of enhanced vorticity is apparent in the midtroposphere near 65-km radius associated with the convergence of M at this level. The azimuthally averaged kinematic structure derived from the ELDORA circumnavigation outside the secondary eyewall at 1838 UTC described here is very similar to the structure derived from the circumnavigation inside the moat at 1801 UTC described by Houze et al. (2007) and Didlake and Houze (2011). This provides confidence that the derived structure is not overly sensitive to the specifics of the flight track.

The changes in the kinematic structure from Figs. 6a to 6b associated with the eyewall replacement over about 23 h are shown in Fig. 6c. A contraction and weakening of the primary eyewall is evident in a vorticity increment dipole at about 20 km, while the remainder of the domain shows increased vorticity that is maximized at the secondary eyewall. The change in transverse circulation shows two tilted gyres centered on the secondary vorticity maximum. If one interprets the vector difference field in Fig. 6c as the secondary circulation induced by the developing secondary eyewall, the response is qualitatively consistent with the EBM. The outward tilt of the gyres is determined by the baroclinity of the vortex. The width of the gyres is dependent on the local Rossby radius of deformation, defined by the ratio of the horizontal gravity wave speed to inertial stability, $L_R = NH/\sqrt{\eta\xi}$, where N is the Brunt–Väisälä frequency, H is the convective scale height, η is the absolute vorticity, and ξ is the modified Coriolis parameter $f + 2\overline{v}/r$. This dynamical length scale determines the radial scale of the compensating subsidence region induced by convective overturning, as well as the approximate width of the transverse streamfunction gyre. If we assume the gravity wave speed $NH \approx 60$ m s^{-1}, associated with deep convective motions (Gill 1980), then the observed 2.4×10^{-3} s^{-1} inertial frequency at the secondary eyewall yields an L_R of about 25-km, similar to the width of the moat region and apparent gyre induced by the secondary eyewall. The corresponding inertial frequency for the primary eyewall is 7.2×10^{-3} s^{-1}, yielding an L_R of about 9 km. These radii are quantitatively consistent with the locations of the eye and moat, where one would expect dynamically constrained subsidence resulting from the superposition of the secondary circulations induced by the two eyewalls. Large radial gradients of tangential wind also contribute to rapid filamentation in these regions, which may contribute further to the lack of convection (Rozoff et al. 2006).

Changes in tangential wind velocity and M in Fig. 6c are centered also at the secondary eyewall, with the zero tendency line near the inner edge of the secondary vorticity maximum. The collocated changes in sign of the vertical, radial, and tangential velocities are closely coupled to the location of the secondary vortex sheet. The tangential wind and M decreased the most near 11-km altitude just outside the RMW. They increased the most from 4- to 10-km altitudes outside the SRMW where substantial midlevel inflow has developed (cf. Fudeyasu and Wang 2011). An integration of the kinetic energy over this domain shows an increase of 19%, similar to that obtained from the 700-hPa in situ data.

Favorable dynamical conditions for sustained convection at 80-km radius, temporal continuity of the 700-hPa kinematic fields, and similarities between the secondary circulation in the outer rainband and secondary eyewall

all support the hypothesis that the vorticity-rich rainband on 21 September was the precursor that developed into the mature secondary eyewall. Ultimately, the discrete observational sampling only allows us to subjectively conclude the temporal continuity of these features, but an unobserved catalyst for the secondary eyewall seems unlikely. Numerical simulations of Rita are consistent also with the interpretation that the secondary eyewall formed near 80-km radius (Judt and Chen 2010; Abarca and Corbosiero 2011).

3) QUAD-DOPPLER ANALYSIS

To examine the flow pattern in more detail, a quad-Doppler analysis was also performed for the period 1801–1820 UTC, just prior to the analysis in Fig. 6b, combining radar data from N42 flying an outbound radial leg at 1.5-km altitude and ELDORA circumnavigating in the moat at 3.6 km. Analysis at this time using ELDORA data only was presented in Houze et al. (2007) and Didlake and Houze (2011). A coarser horizontal grid resolution of 1.5 km was used in the quad-Doppler analysis because of the lower sampling rate of the NOAA tail radar. The flight tracks from this time are shown in Fig. 7, overlaid on the 1.2-km-altitude reflectivity. As described in section 2, the quad-Doppler highly resolved wind field has a reduced uncertainty compared to the dual Doppler analysis due to the nearly orthogonal flight tracks and increased number of independent Doppler velocity measurements. In addition, the low-level in situ data from the N42 radial penetration can be compared to provide additional measurements of the kinematics and augment the analysis with thermodynamic data. The north–south cross section is shown in Fig. 8.[2] Note that this is an individual cross section, not an azimuthal mean, but the good agreement with the kinematic fields and LF radar composite presented earlier suggests a consistent structure that is similar to the azimuthal mean.

The quad-Doppler-derived secondary circulation is quantitatively consistent with Fig. 6b, with an upper-level updraft maximum of about 8 m s^{-1} in the primary eyewall associated with deep convection and a midlevel updraft maximum in the secondary eyewall of about 6 m s^{-1} near the melting level of shallower convection. The moat downdraft is strongest at upper levels (<-2 m s^{-1}) with upper-level convergence, lower-level divergence, and low reflectivity throughout the moat region.

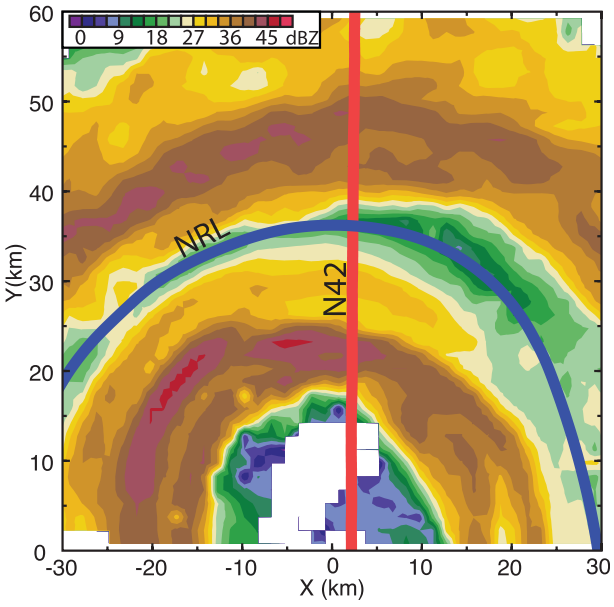

FIG. 7. Quad-Doppler flight tracks during 1801–1821 UTC 22 Sep. The NRL P-3 track is at 3.6 km (blue line) and the N42 P-3 track is at 1.5 km (red line). Reflectivity at 1.2-km altitude is combined from both aircraft.

A portion of the winds at the upper levels along the inner edge of the primary eyewall is also directed into the eye, consistent with the EBM. Outflow is found throughout most of the domain, except at low levels radially outward of the secondary eyewall where there is inflow up to 5-km altitude.

Selected in situ measurements are displayed in Fig. 8b, showing the horizontal wind speed, surface pressure, pseudoequivalent potential temperature, and vertical velocity at 1.5 km. This height is approximately near the top of the boundary layer. The radii bracketing reflectivities greater than 35 dBZ are marked to highlight the agreement between in situ updrafts and downdrafts and the two eyewalls. Seven updrafts exceeded 3 m s^{-1} in these regions. Updrafts along the inner edge of the primary eyewall are consistent with the radar analysis showing the strongest vertical motion in this narrow band as well, similar to findings from other intense storms (cf. Marks and Houze 1987; Marks et al. 2008). A downdraft in the moat less than -1 m s^{-1} is marked by an asterisk, indicating that the subsidence extends to the lower troposphere (cf. Wang 2008). Histograms of vertical velocity from ELDORA flight-level data in the moat are also consistent with the radar-derived magnitudes (not shown). The tangential wind speed in the secondary eyewall is only about 5 m s^{-1} lower than in the primary eyewall at 1.5-km altitude, resulting in a broad region of very high winds. The strong tangential winds are accompanied by a roughly 60-hPa pressure decrease over

[2] The specific layout of this figure was designed to mimic Fig. 3 of Marks et al. (2008). We believe this is a very useful way to display radial hurricane penetration data that allows for intercomparison with other intense tropical cyclones.

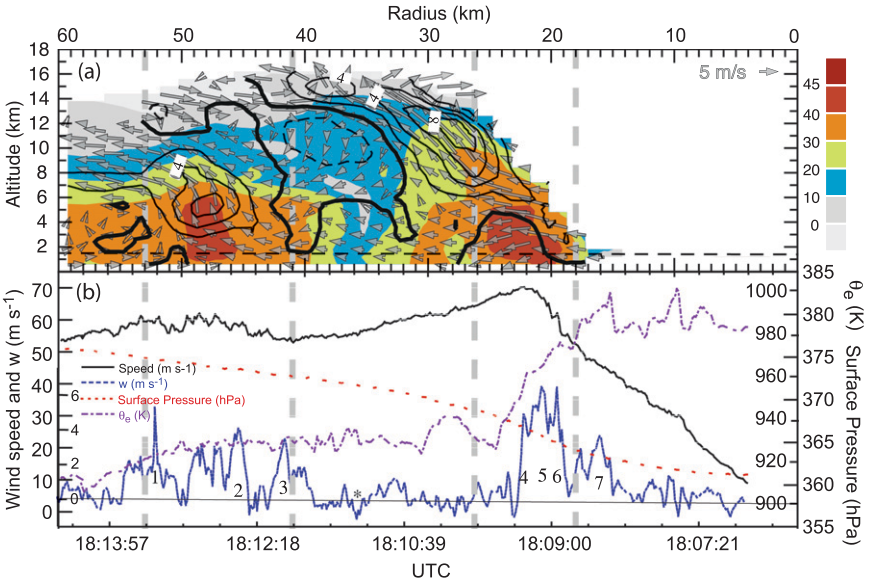

FIG. 8. North–south vertical cross section of quad-Doppler radar analysis from N42 and ELDORA and in situ flight level data at 1.5 km from N42. (a) Radar reflectivity (color), vertical velocity (contour, m s^{-1}), and secondary circulation (vector); (b) wind speed, vertical velocity, surface pressure, and pseudoequivalent potential temperature. Note that axes are reversed to indicate a north–south vertical cross section, not an axisymmetric mean.

60 km to a central pressure of 914 hPa. There is good agreement between the kinematic structures derived from the ELDORA, quad-Doppler, and flight-level data at 700 hPa (~3 km) and 1.5-km altitudes.

The in situ data indicate that the moist entropy was very high in the eye, with pseudoequivalent potential temperature exceeding 380 K. An additional mechanism for intensity change that has been explored recently with numerical modeling (Persing and Montgomery 2003; Cram et al. 2007) and observations (Montgomery et al. 2006a; Bell and Montgomery 2008) concerns the role of the low-level thermodynamics in the eye. Transport of higher entropy air from the eye to the primary eyewall could provide a beneficial heat and buoyancy source (Eastin et al. 2005) for maintaining or increasing convection, although the role of thermodynamic mixing between the eye and eyewall is still under some debate (Bryan and Rotunno 2009; Wang and Xu 2010; Xu and Wang 2010; Barnes and Fuentes 2010). There is a strong moist entropy gradient across the primary eyewall, with a weaker entropy gradient across the secondary eyewall. This is consistent with the view that the lower-tropospheric eyewall exhibits frontal-like characteristics in both θ_e and M (Emanuel 1997).

4. Boundary layer structure

Dropsonde data below 1-km altitude were azimuthally averaged over 10-km annuli centered on the primary and secondary eyewall radii to examine the evolution of the axisymmetric boundary layer. Dropsonde data from each entire IOP (1500–2300 UTC on each day) were included in the averaging to improve the sample size and spatial resolution of the data, with a corresponding loss in temporal resolution. The dropsonde locations and center radii used for averaging are shown in Fig. 9a, and the azimuthally averaged dropsonde data are shown in Figs. 9b–d. The strongest radial inflow is found near the surface at all times, with peak values near hurricane force found at the primary eyewall on 21 September (Fig. 9b). The inflow at 80-km radius is weaker throughout the depth of the boundary layer on this day. On 22 September, the inflow at the primary eyewall has decreased, and the inflow at the secondary ring has increased. Both eyewalls have similar surface inflow of 17 m s^{-1}, but the secondary eyewall at 40 km has a stronger inflow through a deeper layer.

The vertical profiles of tangential winds (Fig. 9c) indicate that the strongest wind velocities are found within the boundary layer in both the primary and secondary eyewalls (cf. Kepert and Wang 2001; Zhang et al. 2001). A weak tangential wind maximum is found below 1-km altitude at 80-km radius in the early period, and increases to a distinct peak at 600-m altitude in the later period. This maximum is at approximately the same altitude as the peak velocity in the primary eyewall on the first day. A decreased peak velocity is evident at 400-m altitude on the second day in the primary eyewall. The

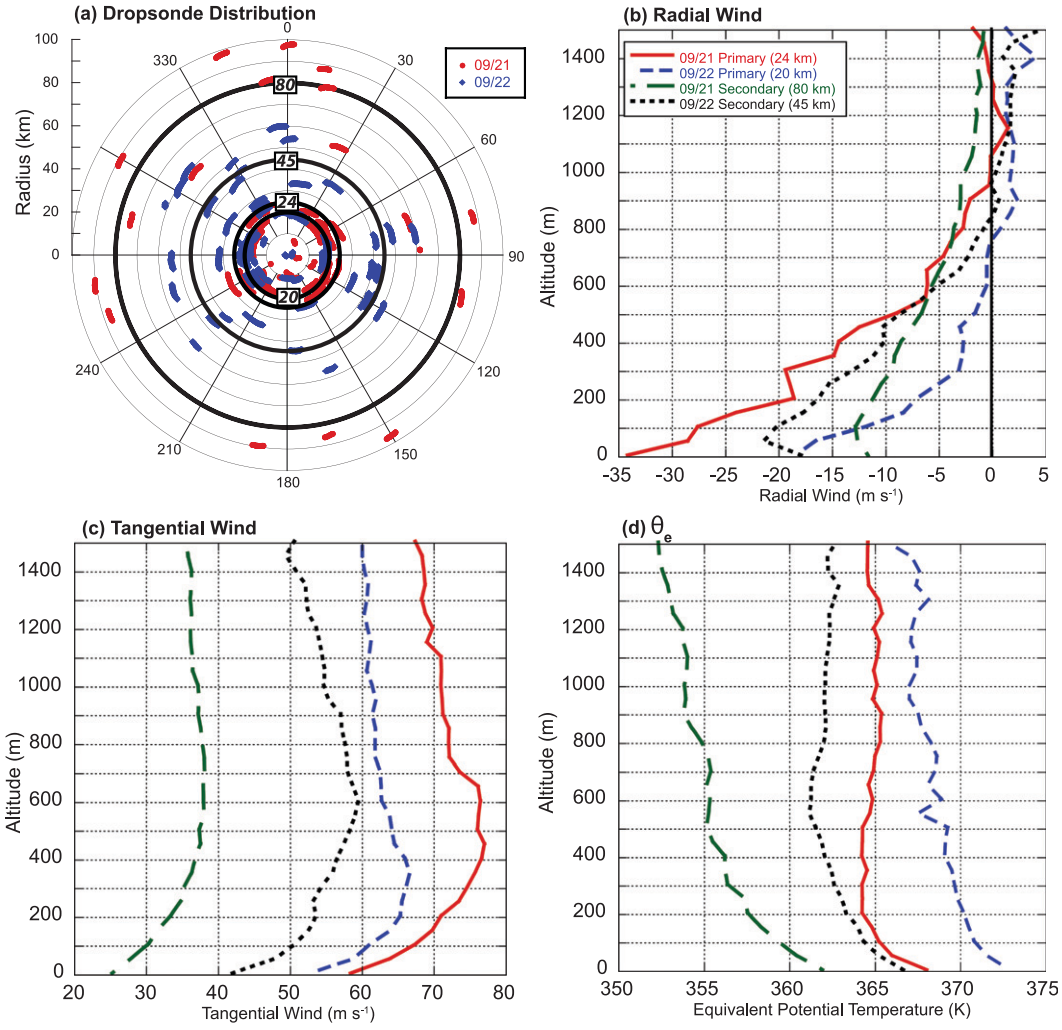

FIG. 9. (a) Storm-relative dropsonde distribution, with red circles indicating sonde locations on 21 Sep and blue diamonds on 22 Sep. Central radii used for azimuthal averaging in 10-km annulus are highlighted and labeled. (b) Azimuthal mean radial wind, (c) mean tangential wind, and (d) mean equivalent potential temperature in each annulus. Red solid line is primary eyewall on 21 Sep, blue dashed line is primary eyewall on 22 Sep, green dash-dotted line is secondary eyewall on 21 Sep, and black dotted line is secondary eyewall on 22 Sep.

decreased intensity of the maximum tangential winds in the primary eyewall is consistent with the decrease in radial inflow and a reduction in the low-level convergence of M. Likewise, the changes in radial and tangential wind are reversed as the secondary eyewall spins up.

The moist entropy structure evolved over this period also (see Fig. 9d). The changes in the magnitude of θ_e are believed to be primarily due to the radial movement of the eyewalls, but the changes in slope of the vertical profiles of θ_e are believed to indicate changes in conditional instability. The vertical profile of θ_e in the primary eyewall evolved from nearly constant with height above the surface layer to a negative slope. In contrast, the secondary eyewall evolved from a negative slope toward a constant with height. This suggests a transition from a conditionally unstable profile toward moist neutrality in the secondary eyewall, and vice versa for the primary eyewall. However, the conditional instability along angular momentum surfaces cannot be directly assessed with these profiles because of the limited altitude sampling and outward tilt of the eyewalls.

The radial structure of the boundary layer is illustrated in Fig. 10a by using a Barnes analysis (Barnes 1973) at 1.5-km horizontal resolution following the methodology described in Montgomery et al. (2006a) and Bell and Montgomery (2008). The composite analysis shows the azimuthal mean θ_e, radial wind, divergence, and agradient acceleration resulting from the radial advection of

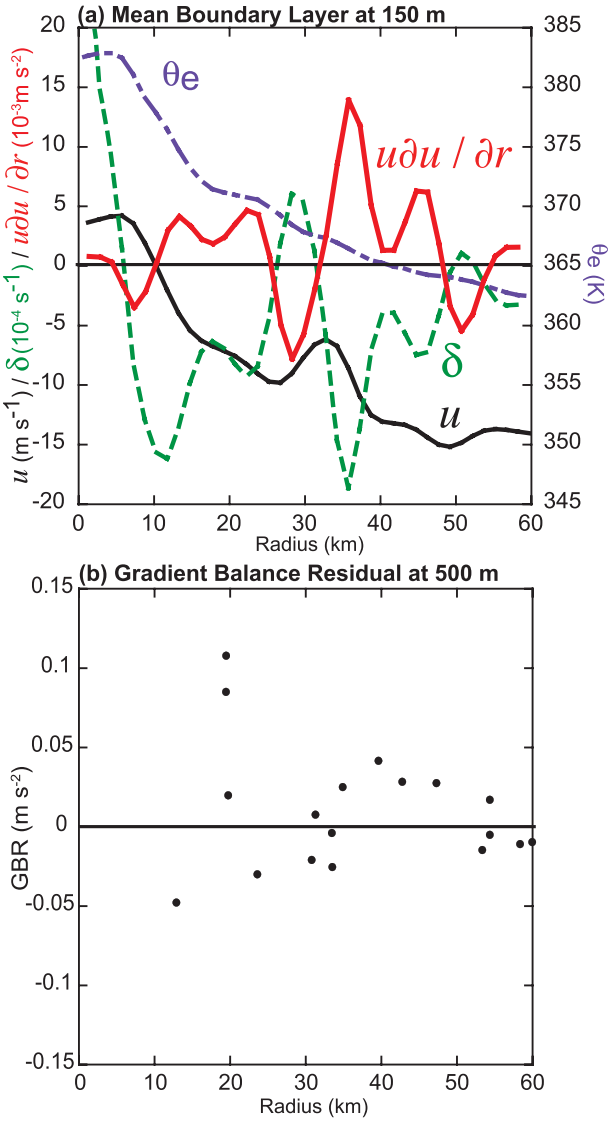

FIG. 10. Boundary layer analysis on 22 Sep. (a) Azimuthal mean radial wind (solid black, m s^{-1}), divergence (green dashed, 10^{-4} s^{-1}), radial advection of the radial wind $u\partial u/\partial r$ (solid red, 10^{-3} m s^{-2}) and pseudoequivalent potential temperature (purple dash-dotted, K) at 150-m altitude. (b) Gradient balance residual at 500 m calculated from dropsondes at different radii from Didlake and Houze (2011).

u at 150-m altitude on 22 September. The radial structure of the azimuthally averaged θ_e derived from the dropsonde measurements is consistent with the in situ data obtained just above the boundary layer, with high values in the eye and the strongest radial gradient at the primary eyewall (cf. Fig. 8). Similar to Fig. 9, the strongest inflow is found at the secondary eyewall, and is reduced toward the primary eyewall, turning to outflow in the eye. Alternating regions of divergence and convergence correspond well to the observed vertical velocity pattern.

The strongest convergence is found a few kilometers radially inwards of the RMW and SRMW, where the radial flow is rapidly decelerated. The deceleration of the radial wind is consistent with an agradient force associated with supergradient winds in both eyewalls. Smaller areas of radial acceleration are apparent in the eye, moat, and outside the secondary eyewall where subgradient winds might be expected. Following the methodology outlined in Bell and Montgomery (2008), Didlake and Houze (2011) calculated the departure from gradient balance at the secondary eyewall using dropsonde data. Their results are reproduced in Fig. 10b, suggesting that the boundary layer tangential winds at 500-m altitude were supergradient in the primary and secondary eyewalls, and subgradient outside the eyewalls. These results are consistent with the radial wind accelerations shown in Fig. 10a.

5. Discussion

The analysis presented provides evidence of an expanding tangential wind field corresponding to the radial convergence of M above the boundary layer throughout the observation period. These observations are consistent with the EBM and the first intensification mechanism, reaffirming their usefulness as a zero-order description of the eyewall intensification process. However, unbalanced dynamics are not captured by the EBM. In contrast to the first mechanism that assumes gradient wind balance, the agradient force associated with supergradient winds in the second mechanism will tend to rapidly decelerate a portion of the inflow in the boundary layer. The deceleration of the radial wind implies increased low-level convergence that, in conjunction with conditional instability, supports deep convection in the secondary eyewall. This deep convection will lead to further intensification by the first mechanism. The strong convergence at 150-m altitude evident in the dropsonde analyses, just radially inward of both eyewalls, supports the foregoing interpretation. The gradient balance residuals at 500 m calculated by Didlake and Houze (2011) and the maximum azimuthally averaged tangential wind speeds near 600-m altitude in both the primary and secondary eyewalls provide further evidence to corroborate this interpretation.

Bui et al. (2009) concluded that the EBM captured a large fraction of the secondary circulation in an idealized three-dimensional hurricane simulation, but also that the EBM underestimated the intensification rate, especially in the boundary layer. Huang et al. (2012) demonstrated that a progressive control by the boundary layer dynamics was an important aspect of secondary eyewall formation in their numerical simulation of

Typhoon Sinlaku. The current analysis does not permit a definitive statement on the relative importance of the two spinup mechanisms, but our results are not inconsistent with Bui et al.'s (2009) or Huang et al.'s (2012) interpretations. Further analysis of the quantitative degree of super- and subgradient winds depends on careful analysis of the pressure field, vertical advection of the radial wind, and assumptions about unresolved turbulent fluxes. A more detailed attribution of the spinup process from the balanced and unbalanced processes requires several additional assumptions about missing data in the eye and boundary layer, frictional forces, diabatic heating fields, and thermodynamic gradients that go far beyond the scope of the current study.

The two axisymmetric spinup mechanisms described herein do not specifically address the decay of the primary eyewall, nor do they address where and when a secondary eyewall will form. It is difficult to distinguish eyewall formation, maturation, and decay with the temporal resolution of the RAINEX observations.[3] However, this analysis suggests that the main reason for the decay of the inner eyewall is a reduction in the inflow to the primary eyewall as opposed to the direct effects of forced subsidence (Rozoff et al. 2008; Zhou and Wang 2011). Deep subsidence is observed in the moat where the downward branches of the independent secondary circulations coincide, but the radar analysis suggests that forced subsidence from the secondary eyewall is not strong enough to significantly suppress deep convection at the primary eyewall. The primary eyewall updraft is weaker and more asymmetric on the second analysis day, but it is still deeper and more vigorous than the secondary eyewall updraft. The boundary layer inflow and low-level convergence increased at the secondary eyewall as it matured, while the inflow at the primary eyewall decreased. At 700 hPa the inward movement of the M surfaces just outside the primary eyewall was reversed. This led to a spindown of the primary eyewall both within and above the boundary layer, but it remained the dominant eyewall throughout the analysis period.

The precursor to Rita's secondary eyewall formation was estimated to be a vorticity-rich rainband near 80-km radius on 21 September. Reduced radial shear of the tangential velocity in this region is consistent with long filamentation times and an increased likelihood for sustained convection (Rozoff et al. 2006). Limitations of the dataset do not preclude the idea that the secondary eyewall originated even earlier and/or radially outward of this location, but satellite imagery (Fig. 2a) does not suggest that there were any significant convective structures prior to this time other than the principal rainband. Satellite and radar imagery suggest that the principal rainband had propagated radially outward from this location and was decaying at this time. The precursor rainband identified in this study appeared to be a distinct feature, suggesting that the primary rainband itself did not directly transform into the secondary eyewall. However, the location of the primary rainband near the precursor region suggests that it may have played a role in preconditioning and/or determining the location of secondary eyewall formation and bears further study. Additional observations at an earlier stage of secondary eyewall formation are recommended.

The enhanced vorticity in the precursor rainband is compatible with the concept of a vortex Rossby wave (VRW) that propagates on the mean radial potential vorticity gradient, analogous to planetary Rossby waves on the meridional beta plane (Montgomery and Kallenbach 1997; Chen and Yau 2001; Wang 2002a,b; Corbosiero et al. 2006). Recent interpretations of numerical simulations are varied on the importance and role of VRW activity in secondary eyewall formation and evolution (Terwey and Montgomery 2008; Wang 2009; Martinez et al. 2010; Qiu et al. 2010; Judt and Chen 2010; Abarca and Corbosiero 2011; Huang et al. 2012). Whether the primary effect of VRWs is to contribute primarily to the azimuthally averaged latent heating, spinup or spindown of the vortex through eddy-vorticity and eddy-heat fluxes, or providing a favored location for secondary eyewall formation remains an important open question. Didlake and Houze (2011) demonstrated that vorticity tendencies in Rita's secondary eyewall due to the perturbation terms were nonnegligible, and bear further study. A more thorough analysis of VRWs and asymmetric processes with the RAINEX dataset is recommended for future work.

Additionally, the role of eyewall replacement in a tropical cyclone's life cycle is still not fully understood. After the analysis period documented in this study, Rita weakened to category 3 intensity and underwent an additional eyewall replacement cycle in an environment with moderate vertical shear and high ocean-heat content. This contrasts with the life cycle of Hurricane Isabel (2003), which displayed an expanding eyewall that stayed at or near category 5 intensity for three consecutive days (Bell and Montgomery 2008) in a low vertical shear, low ocean heat content environment (Mainelli et al. 2008). The reasons for these different evolutions are not currently well understood but may include differences in environmental influences (Nong and Emanuel 2003) or microphysical processes (Zhou and Wang 2011; Zhou et al. 2011).

[3] Ultimately, there is a continuum of evolving states in the TC life cycle and such a distinction may not be all that meaningful.

6. Summary

Multiplatform analyses of observations from RAINEX have provided a unique look at Hurricane Rita's concentric eyewall evolution. The expansion of the tangential wind field is believed to have contributed to a region possessing a relatively large filamentation time that was dynamically favorable for deep convection near 80-km radius. A vorticity-rich rainband near this region intensified and contracted over the 24-h analysis period to form the secondary eyewall. The results presented herein indicate that the maturing secondary eyewall exhibited increasing tangential wind speeds, an intensifying and deepening secondary circulation, and a more symmetric convective ring over the analysis period. The low-level radial gradients of absolute angular momentum and moist entropy were sharpened also over this time.

The secondary eyewall took on these intensifying characteristics as the primary eyewall deteriorated and was eventually replaced. However, the primary eyewall was still very intense and was the dominant swirling wind and vorticity structure at the end of the analysis period. The moat region in between the two eyewalls developed characteristics of a hurricane eye (Houze et al. 2007), with radially constrained subsidence that appears to be the result of a combined forcing from both eyewalls. The width of observed secondary circulation gyres is consistent with the local Rossby radius of deformation estimated from the dual- and quad-Doppler radar analysis. The qualitative agreement between the theoretical predictions of the Eliassen balance model and the analyses presented herein suggests that this framework provides a useful description of the slowly evolving secondary circulation above the boundary layer.

The axisymmetric spinup of the secondary eyewall is associated with radial convergence of absolute angular momentum above and within the boundary layer. Above the boundary layer, M is approximately conserved materially as it is advected toward the developing eyewall in the low to midtroposphere by a deep layer of weak radial inflow that is argued to be a result of diabatic heating in the intensifying convective ring. Inflow above the boundary layer is evident in the radar observations, and the analysis presented here indicates that Rita's hurricane-force winds increased in area by 125% and the integrated kinetic energy increased by 19% after peak intensity. This result is qualitatively consistent with the theoretical predictions of axisymmetric balance theory.

Although M is not materially conserved in the boundary layer due to the azimuthal torque associated with surface friction, spinup of the boundary layer tangential wind that may exceed interior values can occur if the radial inflow is sufficiently large to converge rings of air to small radii with minimal loss of M. The generation of supergradient winds leads to a rapid deceleration of inflow in the boundary layer that, in conjunction with conditional instability, supports deep convection in the secondary eyewall and further intensification. The analyses presented indicate that strong convergence, gradient wind imbalance, and a maximum in tangential winds were found in the boundary layer, accompanied by an eruption of air and low-level radial outflow above the boundary layer. An increase in frictional inflow and associated low-level convergence over the analysis period suggests that unbalanced boundary layer dynamics may have become progressively important as the secondary eyewall matured. Although a detailed separation of the contributions from balanced and unbalanced processes is beyond the scope of the present study, the observations presented herein suggest that both balanced and unbalanced intensification mechanisms were important in Rita's eyewall replacement. The analyses support the two axisymmetric mechanisms proposed by Smith et al. (2009) and Montgomery and Smith (2011, manuscript submitted to *Quart. J. Roy. Meteor. Soc.*) as a useful framework for understanding concentric eyewall evolution.

The analyses here provide new evidence that changes in heating, moist entropy, toroidal and vertical vorticity, and ultimately wind speed are concurrent and highly coupled in a developing secondary eyewall. While the axisymmetric view has been shown to be quite useful for gaining insight into the processes responsible for these changes, the observations suggest also that nonaxisymmetric contributions must be included for a complete understanding of eyewall evolution. Additional observations and further basic research on the topic of secondary eyewall formation and evolution are advocated to improve our understanding and forecasts of the phenomenon and related size expansions of intense tropical cyclones.

Acknowledgments. The authors would like to acknowledge the National Science Foundation for supporting the RAINEX experiment and National Center for Atmospheric Research, and the many participants who made the project a success. We would like to specifically thank Robert Houze and Bradley Smull for their expertise in the field and helpful comments during the early phase of this research; Kristen Corbosiero for providing the vertical shear calculations; Anthony Didlake for providing the gradient balance residuals; and Sergio Abarca, Michael Riemer, Yuqing Wang, and two anonymous reviewers for their comments on the manuscript. MMB and WCL were supported by NCAR-EOL, which is supported by the National Science Foundation. MTM acknowledges the support of Grant N00014-03-1-0185 from the U.S.

Office of Naval Research, NOAA's Hurricane Research Division, and the National Science Foundation NSF AGS-0733380 and AGS-0715426.

REFERENCES

Abarca, S. F., and K. L. Corbosiero, 2011: Secondary eyewall formation in WRF simulations of Hurricanes Rita and Katrina (2005). *Geophys. Res. Lett.,* **38,** L07802, doi:10.1029/2011GL047015.

Barnes, G. M., and P. Fuentes, 2010: Eye excess energy and the rapid intensification of Hurricane Lili (2002). *Mon. Wea. Rev.,* **138,** 1446–1458.

Barnes, S. L., 1973: Mesoscale objective analysis using weighted time-series observations. NOAA Tech. Memo. ERL NSSL-62, 60 pp.

Bell, M. M., and M. T. Montgomery, 2008: Observed structure, evolution, and potential intensity of category 5 Hurricane Isabel (2003) from 12 to 14 September. *Mon. Wea. Rev.,* **136,** 2023–2046.

Beven, J. L., and Coauthors, 2008: Atlantic hurricane season of 2005. *Mon. Wea. Rev.,* **136,** 1109–1173.

Black, M. L., and H. E. Willoughby, 1992: The concentric eyewall cycle of Hurricane Gilbert. *Mon. Wea. Rev.,* **120,** 947–957.

Bolton, D., 1980: The computation of equivalent potential temperature. *Mon. Wea. Rev.,* **108,** 1046–1053.

Bosart, B. L., W. C. Lee, and R. M. Wakimoto, 2002: Procedures to improve the accuracy of airborne Doppler radar data. *J. Atmos. Oceanic Technol.,* **19,** 322–339.

Bryan, G. H., and R. Rotunno, 2009: The influence of near-surface, high-entropy air in hurricane eyes on maximum hurricane intensity. *J. Atmos. Sci.,* **66,** 148–158.

Bui, H. H., R. K. Smith, and M. T. Montgomery, 2009: Balanced and unbalanced aspects of tropical-cyclone intensification. *Quart. J. Roy. Meteor. Soc.,* **135,** 1715–1731.

Chen, Y., and M. K. Yau, 2001: Spiral bands in a simulated hurricane. Part I: Vortex Rossby wave verification. *J. Atmos. Sci.,* **58,** 2128–2145.

Corbosiero, K. L., and J. Molinari, 2002: The effects of vertical wind shear on the distribution of convection in tropical cyclones. *Mon. Wea. Rev.,* **130,** 2110–2123.

——, ——, A. R. Aiyyer, and M. L. Black, 2006: The structure and evolution of Hurricane Elena (1985). Part II: Convective asymmetries and evidence for vortex Rossby waves. *Mon. Wea. Rev.,* **134,** 3073–3091.

Cram, T. A., J. Persing, M. T. Montgomery, and S. A. Braun, 2007: A Lagrangian trajectory view on transport and mixing processes between the eye, eyewall and environment using a high-resolution simulation of Hurricane Bonnie (1998). *J. Atmos. Sci.,* **64,** 1835–1857.

Didlake, A. C., Jr., and R. A. Houze Jr., 2011: Kinematics of the secondary eyewall observed in Hurricane Rita (2005). *J. Atmos. Sci.,* **68,** 1620–1636.

Dodge, P., R. W. Burpee, and F. D. Marks, 1999: The kinematic structure of a hurricane with sea level pressure less than 900 mb. *Mon. Wea. Rev.,* **127,** 987–1004.

Eastin, M. D., P. G. Black, and W. M. Gray, 2002: Flight-level instrument wetting errors in hurricanes. Part I: Observations. *Mon. Wea. Rev.,* **130,** 825–841.

——, W. M. Gray, and P. G. Black, 2005: Buoyancy of convective vertical motions in the inner core of intense hurricanes. Part I: General statistics. *Mon. Wea. Rev.,* **133,** 188–208.

Eliassen, A., 1952: Slow thermally or frictionally controlled meridional circulation in a circular vortex. *Astrophys. Norv.,* **5,** 19–60.

Elsberry, R. L., and R. A. Stenger, 2008: Advances in understanding of tropical wind structure changes. *Asia–Pac. J. Atmos. Sci.,* **44,** 11–24.

Emanuel, K. A., 1997: Some aspects of hurricane inner-core dynamics and energetics. *J. Atmos. Sci.,* **54,** 1014–1026.

Fang, J., and F. Zhang, 2010: Initial development and genesis of Hurricane Dolly (2008). *J. Atmos. Sci.,* **67,** 655–672.

Franklin, J., M. L. Black, and K. Valde, 2003: GPS dropwindsonde wind profiles in hurricanes and their operational implications. *Wea. Forecasting,* **18,** 32–44.

Fudeyasu, H., and Y. Wang, 2011: Balanced contribution to the intensification of a tropical cyclone simulated in TCM4: Outer core spinup process. *J. Atmos. Sci.,* **68,** 430–449.

——, ——, M. Satoh, T. Nasuno, H. Miura, and W. Yanase, 2010: Multiscale interactions in the life cycle of a tropical cyclone simulated in a global cloud-system-resolving model. Part II: System-scale and mesoscale processes. *Mon. Wea. Rev.,* **138,** 4305–4327.

Gao, J., M. Xue, A. Shapiro, and K. K. Droegemeier, 1999: A variational method for the analysis of three-dimensional wind fields from two Doppler radars. *Mon. Wea. Rev.,* **127,** 2128–2142.

Gill, A. E., 1980: Some simple solutions for heat-induced tropical circulation. *Quart. J. Roy. Meteor. Soc.,* **106,** 447–462.

Hawkins, J. D., and M. Helveston, 2008: Tropical cyclone multiple eyewall characteristics. *Extended Abstracts, 28th Conf. on Hurricanes and Tropical Meteorology,* Orlando, FL, Amer. Meteor. Soc., 14B.1. [Available online at http://ams.confex.com/ams/28Hurricanes/techprogram/paper_138300.htm.]

Hence, D. A., and R. A. Houze, 2008: Kinematic structure of convective-scale elements in the rainbands of Hurricanes Katrina and Rita (2005). *J. Geophys. Res.,* **113,** D15108, doi:10.1029/2007JD009429.

Hendricks, E. A., M. T. Montgomery, and C. A. Davis, 2004: The role of "vortical" hot towers in the formation of Tropical Cyclone Diana (1984). *J. Atmos. Sci.,* **61,** 1209–1232.

Hildebrand, P. H., and Coauthors, 1996: The ELDORA/ASTRAIA airborne Doppler weather radar: High-resolution observations from TOGA COARE. *Bull. Amer. Meteor. Soc.,* **77,** 213–232.

Hock, T. F., and J. L. Franklin, 1999: The NCAR GPS dropwindsonde. *Bull. Amer. Meteor. Soc.,* **80,** 407–420.

Houze, R. A., and Coauthors, 2006: The Hurricane Rainband and Intensity Change Experiment: Observations and modeling of Hurricanes Katrina, Ophelia, and Rita. *Bull. Amer. Meteor. Soc.,* **87,** 1503–1521.

——, S. S. Chen, B. F. Smull, W.-C. Lee, and M. M. Bell, 2007: Hurricane intensity and eyewall replacement. *Science,* **315,** 1235–1239.

——, W.-C. Lee, and M. M. Bell, 2009: Convective contribution to the genesis of Hurricane Ophelia (2005). *Mon. Wea. Rev.,* **137,** 2778–2800.

Huang, Y.-H., M. T. Montgomery, and C.-C. Wu, 2012: Concentric eyewall formation in Typhoon Sinlaku (2008). Part II: Axisymmetric dynamical processes. *J. Atmos. Sci.,* **69,** 662–674.

Jorgensen, D. P., T. Mateka, and J. D. DuGranrut, 1996: Multibeam techniques for deriving wind fields from airborne Doppler radars. *Meteor. Atmos. Phys.,* **59,** 83–104.

Judt, F., and S. S. Chen, 2010: Convectively generated potential vorticity in rainbands and formation of the secondary eyewall in Hurricane Rita of 2005. *J. Atmos. Sci.,* **67,** 3581–3599.

Kepert, J. D., and Y. Wang, 2001: The dynamics of boundary layer jets within the tropical cyclone core. Part II: Nonlinear enhancement. *J. Atmos. Sci.,* **58,** 2485–2501.

Leise, J. A., 1982: A multidimensional scale-telescoped filter and data extension package. NOAA Tech. Memo. ERL WPL-82, 19 pp.

Maclay, K. S., M. DeMaria, and T. H. Vonder Haar, 2008: Tropical cyclone inner-core kinetic energy evolution. *Mon. Wea. Rev.,* **132,** 4882–4898.

Mainelli, M., M. DeMaria, L. K. Shay, and G. Goni, 2008: Application of oceanic heat content estimation to operational forecasting of recent Atlantic category 5 hurricanes. *Wea. Forecasting,* **23,** 3–16.

Marks, F. D., 1985: Evolution of the structure of precipitation in Hurricane Allen (1980). *Mon. Wea. Rev.,* **113,** 909–930.

——, and R. A. Houze, 1987: Airborne Doppler radar observations in Hurricane Debby. *Bull. Amer. Meteor. Soc.,* **65,** 569–582.

——, ——, and J. F. Gamache, 1992: Dual-aircraft investigation of the inner core of Hurricane Norbert. Part I: Kinematic structure. *J. Atmos. Sci.,* **49,** 919–942.

——, P. G. Black, M. T. Montgomery, and R. W. Burpee, 2008: Structure of the eye and eyewall of Hurricane Hugo (1989). *Mon. Wea. Rev.,* **136,** 1237–1259.

Martinez, Y., G. Brunet, and M. K. Yau, 2010: On the dynamics of two-dimensional hurricane-like concentric rings vortex formation. *J. Atmos. Sci.,* **67,** 3253–3268.

Melander, M. V., J. C. McWilliams, and N. J. Zabusky, 1987: Axisymmetrization and vorticity-gradient intensification of an isolated two-dimensional vortex through filamentation. *J. Fluid Mech.,* **178,** 137–159.

Montgomery, M. T., and R. J. Kallenbach, 1997: A theory for vortex Rossby-waves and its application to spiral bands and intensity change in hurricanes. *Quart. J. Roy. Meteor. Soc.,* **538,** 435–465.

——, M. M. Bell, S. D. Aberson, and M. Black, 2006a: Superintense winds in Hurricane Isabel (2003). Part I: Mean vortex structure and maximum intensity estimates. *Bull. Amer. Meteor. Soc.,* **87,** 1335–1347.

——, M. E. Nicholls, T. A. Cram, and A. B. Saunders, 2006b: A vortical hot tower route to tropical cyclogenesis. *J. Atmos. Sci.,* **63,** 355–386.

Nguyen, V. S., R. K. Smith, and M. T. Montgomery, 2008: Tropical cyclone intensification and predictability in three dimensions. *Quart. J. Roy. Meteor. Soc.,* **134,** 563–582.

Nong, S., and K. Emanuel, 2003: A numerical study of the genesis of concentric eyewalls in hurricanes. *Quart. J. Roy. Meteor. Soc.,* **129,** 3323–3338.

Ooyama, K. V., 1982: Conceptual evolution of the theory and modeling of the tropical cyclone. *J. Meteor. Soc. Japan.,* **60,** 369–380.

Oye, R., C. Mueller, and S. Smith, 1995: Software for radar translation, visualization, editing, and interpolation. Preprints, *27th Conf. on Radar Meteorology,* Vail, CO, Amer. Meteor. Soc., 359–361.

Persing, J., and M. T. Montgomery, 2003: Hurricane superintensity. *J. Atmos. Sci.,* **60,** 2349–2371.

Powell, M. D., and T. A. Reinhold, 2007: Tropical cyclone destructive potential by integrated kinetic energy. *Bull. Amer. Meteor. Soc.,* **88,** 513–526.

Qiu, X., Z.-M. Tan, and Q. Xiao, 2010: The roles of vortex Rossby waves in hurricane secondary eyewall formation. *Mon. Wea. Rev.,* **138,** 2092–2109.

Reasor, P. D., M. D. Eastin, and J. F. Gamache, 2009: Rapidly intensifying Hurricane Guillermo (1997). Part I: Low-wavenumber structure and evolution. *Mon. Wea. Rev.,* **137,** 603–631.

Rozoff, C. M., W. H. Schubert, B. D. McNoldy, and J. P. Kossin, 2006: Rapid filamentation zones in intense tropical cyclones. *J. Atmos. Sci.,* **63,** 325–340.

——, ——, and J. P. Kossin, 2008: Some dynamical aspects of tropical cyclone concentric eyewalls. *Quart. J. Roy. Meteor. Soc.,* **134,** 583–593.

Schubert, W. H., and J. J. Hack, 1982: Inertial stability and tropical cyclone development. *J. Atmos. Sci.,* **39,** 1687–1697.

——, and ——, 1983: Transformed Eliassen balanced vortex model. *J. Atmos. Sci.,* **40,** 1571–1583.

Shapiro, L. J., and H. E. Willoughby, 1982: The response of hurricanes to balanced sources of heat and momentum. *J. Atmos. Sci.,* **49,** 378–394.

——, and M. T. Montgomery, 1993: A three-dimensional balance theory for rapidly rotating vortices. *J. Atmos. Sci.,* **50,** 3322–3335.

Smith, R. K., 1981: The cyclostrophic adjustment of vortices with application to tropical cyclone modification. *J. Atmos. Sci.,* **38,** 2021–2030.

——, and M. T. Montgomery, 2010: Hurricane boundary-layer theory. *Quart. J. Roy. Meteor. Soc.,* **136,** 1665–1670.

——, ——, and S. Vogl, 2008: A critique of Emanuel's hurricane model and potential intensity theory. *Quart. J. Roy. Meteor. Soc.,* **134,** 551–561.

——, ——, and N. Van Sang, 2009: Tropical cyclone spin-up revisited. *Quart. J. Roy. Meteor. Soc.,* **135,** 1321–1335.

Terwey, W. D., and M. T. Montgomery, 2008: Secondary eyewall formation in two idealized, full-physics modeled hurricanes. *J. Geophys. Res.,* **113,** D12112, doi:10.1029/2007JD008897.

Wang, Y., 2002a: Vortex Rossby waves in a numerically simulated tropical cyclone. Part I: Overall structure, potential vorticity, and kinetic energy budgets. *J. Atmos. Sci.,* **59,** 1213–1238.

——, 2002b: Vortex Rossby waves in a numerically simulated tropical cyclone. Part II: The role in tropical cyclone structure and intensity changes. *J. Atmos. Sci.,* **59,** 1239–1262.

——, 2008: Rapid filamentation zone in a numerically simulated tropical cyclone. *J. Atmos. Sci.,* **65,** 1158–1181.

——, 2009: How do outer spiral rainbands affect tropical cyclone structure and intensity? *J. Atmos. Sci.,* **66,** 1250–1273.

——, and J. Xu, 2010: Energy production, frictional dissipation, and maximum intensity of a numerically simulated tropical cyclone. *J. Atmos. Sci.,* **67,** 97–116.

Willoughby, H. E., 1979: Forced secondary circulations in hurricanes. *J. Geophys. Res.,* **84,** 3173–3183.

——, J. Clos, and M. Shoreibah, 1982: Concentric eye walls, secondary wind maxima, and the evolution of the hurricane vortex. *J. Atmos. Sci.,* **39,** 395–411.

Xu, J., and Y. Wang, 2010: Sensitivity of the simulated tropical cyclone inner-core size to the initial vortex size. *Mon. Wea. Rev.,* **138,** 4135–4157.

Zhang, D.-L., Y. Liu, and M. K. Yau, 2001: A multiscale numerical study of Hurricane Andrew (1992). Part IV: Unbalanced flows. *Mon. Wea. Rev.,* **129,** 92–107.

Zhang, J. A., R. F. Rogers, D. S. Nolan, and F. D. Marks Jr., 2011: On the characteristic height scales of the hurricane boundary layer. *Mon. Wea. Rev.,* **139,** 2523–2535.

Zhou, X.-Q., and B. Wang, 2011: Mechanism of concentric eyewall replacement cycles and associated intensity change. *J. Atmos. Sci.,* **68,** 972–988.

——, ——, X.-Y. Ge, and T. Li, 2011: Impact of secondary eyewall heating on tropical cyclone intensity change. *J. Atmos. Sci.,* **68,** 450–456.

Zipser, E. J., R. J. Meitin, and M. A. LeMone, 1981: Mesoscale motion fields associated with a slowly moving GATE convective band. *J. Atmos. Sci.,* **38,** 1725–1750.